

國立臺灣大學 理學院物理學研究所

碩士學位論文

Graduate Institute of Physics

College of Science

National Taiwan University

Master Thesis

在KOTO實驗中尋找無質量暗光子： $K_L^0 \rightarrow \gamma\bar{\gamma}$

Search for a massless dark photon in $K_L^0 \rightarrow \gamma\bar{\gamma}$ at the
KOTO Experiment

吳桐

Tong Wu

指導教授：熊怡 教授

Advisor: Yee Bob Hsiung, Ph.D.

中華民國113年8月

August 2024

NATIONAL TAIWAN UNIVERSITY

MASTER THESIS

**Search for a massless dark photon in
 $K_L^0 \rightarrow \gamma\bar{\gamma}$ at the KOTO Experiment**

Author:

Tong Wu

Supervisor:

Dr. Yee Bob HSIUNG

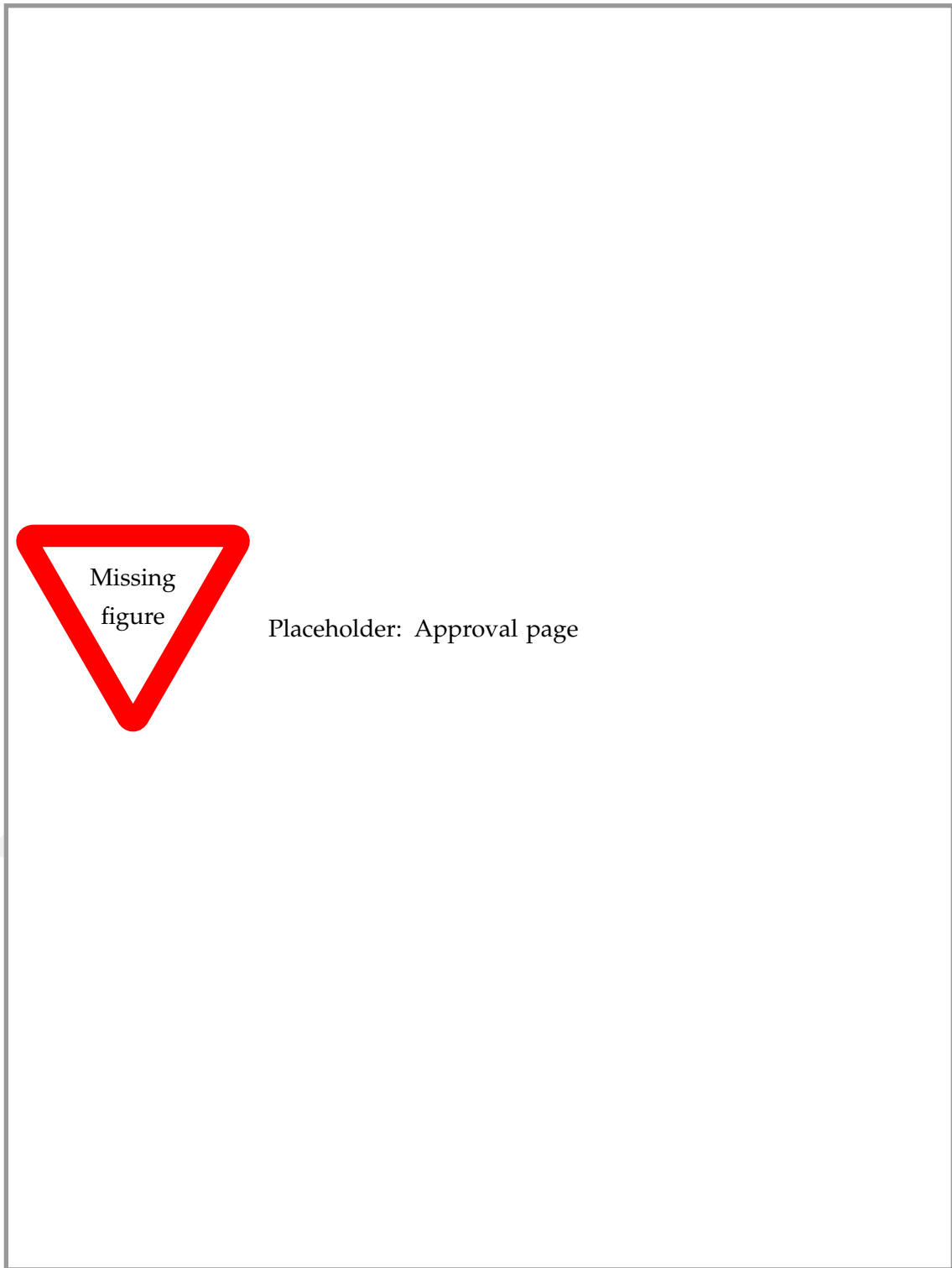


June 27, 2024

© 2024, by Tong Wu
tong@hep1.phys.ntu.edu.tw



ALL RIGHTS RESERVED



Acknowledgements

Thanks all

DRAFT

中文摘要

一二三

三二一

關鍵詞：暗光子、新物理。

Abstract

This thesis presents the search for the massless dark photon ($\bar{\gamma}$) in the $K_L^0 \rightarrow \gamma\bar{\gamma}$ decay at the J-PARC KOTO experiment, based on the special data collected in 2020.

Distinguished from the massive dark photon, the massless one does not directly mix with the ordinary photon but could interact with Standard Model (SM) particles through direct coupling to quarks. Some theoretical models propose that the branching ratio (\mathcal{BR}) of the $K_L^0 \rightarrow \gamma\bar{\gamma}$ decay could reach up to $\mathcal{O}(10^{-3})$.

The number of K_L^0 decays that had been collected in the special run is estimated to be $(1.29 \pm 0.02_{stat.}) \times 10^{10}$. The single event sensitivity is calculated to be $(2.91 \pm 0.02_{stat.}) \times 10^{-8}$. The total background level prediction is $(12.65 \pm 4.61_{stat.})$ with the agreement from the side-band region. We uncovered the blind region and observed 13 events. The Feldman-Cousins method is used to calculate the upper limit of the $K_L^0 \rightarrow \gamma\bar{\gamma}$ branching ratio to be $< 2.15 \times 10^{-7}$ (90%C.L.).

Keywords: Dark Photon, beyond Standard Model.

Contents

Approval	i
Acknowledgements	iii
中文摘要	v
Abstract	vii
Contents	ix
List of Figures	xi
List of Tables	xiii
1 Introduction	1
1.1 Motivation	1
1.2 Dark Photon	1
2 KOTO Experiment	3
2.1 Introduction	3
2.2 $K_L \rightarrow \pi^0 \nu \bar{\nu}$	3
2.3 Beam Line	3
2.4 Detectors	3
2.4.1 CsI	3
2.4.2 Barrel Veto	6
2.4.3 CV	6
2.4.4 Other Veto	6
2.5 Data Acquisition System	6
2.6 Data Taking	6
2.7 Trigger	6
2.8 Basic Strategy of the Single Cluster Study	6
2.8.1 Signal Identification	6
2.8.2 Major Background Sources	6
3 Event Reconstruction	9
3.1 Cluster Finding	9
3.2 Veto Hit Reconstruction	9
3.3 MPPC calibration	9
3.3.1 Cosmic Ray analysis	9
3.3.2 T0 correction	9

3.3.3 $K_L^0 \rightarrow 3\pi^0$ correction	9
4 K_L^0 Yield Estimation	11
4.1 Data Set	11
4.2 Event Selections	12
4.2.1 Veto Cut	12
4.2.2 Kinematic Cut	13
4.3 Yield Estimation	14
4.3.1 Estimation by $K_L^0 \rightarrow 3\pi^0$ Decays	14
5 Monte Carlo Simulation	17
5.1 GEANT4	17
5.2 Accidental Overlay	17
5.3 Beamline simulation	17
5.4 Other Simulations	17
5.4.1 NCC background	17
5.4.2 Halo Kaon	17
5.4.3 Charge Kaon	17
6 Analysis of $K_L \rightarrow \gamma\bar{\gamma}$	19
6.1 Event Selection	20
6.1.1 Trigger Selection	20
6.1.2 Kinematic Cuts	21
6.1.3 Veto Cuts	23
6.2 Background Suppression	23
6.2.1 K_L Decay Background	23
6.2.2 Hadronic Background	26
6.2.3 Low Radius Event background	29
6.3 Single Event Sensitivity	30
6.3.1 Systematic Uncertainty of SES	31
6.4 Background Level Estimation	31
6.5 Unblind and Results	31
6.6 Massive Dark Photon Search	31
7 Conclusion and Discussion	33
7.1 blah	33
Bibliography	35

List of Figures

2.1	The entire view of J-PARC. [2]	4
2.2	Beamline layout	4
2.3	CsI layout	5
2.4	KOTO detector layout	5
4.1	Distribution of isolated crystal hit energy(E) vs. its distance(D) from the nearest cluster. The red line shows the cut based on Equation 4.1. The sample was obtained from the $K_L^0 \rightarrow \pi^0 \nu \bar{\nu}$ Monte Carlo simulation. Figure courtesy of [4]	13
4.2	Distribution of the kinematic variables for the $K_L^0 \rightarrow 3\pi^0$ decay. All the selections are applied except the variable shown in the plot. The black point shows the data, and the fill histogram shows the Monte Carlo simulation. The red arrow indicates the cut-off value of the variable.	15
4.3	Distribution of the kinematic variables for the $K_L^0 \rightarrow 3\pi^0$ decay. All the selections are applied except the variable shown in the plot. The black point shows the data, and the fill histogram shows the Monte Carlo simulation. The red arrow indicates the cut-off value of the variable.	16
6.1	Distribution of cluster timing after relative timing correction. The dot is from real physics data, and the filled histogram is the MC simulation. The red arrow is the cut-off region.	21
6.2	Distribution of total energy from Monte Carlo simulation. The histogram area is normalized to 1. The red arrow is the cut-off region.	21
6.3	An upstream view of the CsI calorimeter. The red region is the outermost boundary, while the blue region is the innermost boundary.	22
6.4	Temporary plots of FBAR and NCC	24
6.5	The schematic geometry diagram of the mechanism of the upstream decay background.	25
6.6	Todo-Fig: Change A B region in different color	
6.7	$E_\gamma - R_{XY}$ distributions of scattered $K_L^0 \rightarrow 2\gamma$ decays with various cut. The red frame indicates the signal region. The red number indicates the background level in each region.	25
6.7	The schematic geometry diagram of the mechanism of the fusion cluster background.	26

6.8	Present the upper limit at 90% confidence level.	
<i>E_γ – R_{XY}</i> distributions of various background sources after applying all selection cuts. Left-hand side plots exclude the neutron cuts and the right-hand side plots include it. The red frame indicates the signal region. The red number indicates the background level in each region.		27
6.9	The architecture of CSD neural network training process.	28
6.10	Distribution of the likelihood ratio for hadronic cluster events (red) and photon cluster events (blue). The photon cluster events are obtained through the $K_L^0 \rightarrow 3\pi^0$ decay analysis of data. The neutron sample is obtained from neutron data.	29
6.11	Illustration of shower depth means. An MPPC is installed on the upstream side. The time difference between the photon arriving upstream and downstream ($\Delta T = T_{MPPC} - T_{PMT}$) is used to measure the depth of the reaction and distinguish between photon events (left) and neutron events (right).	29
6.12	Distribution of the ΔT for neutron events and photon events. The photon cluster events are obtained through the $K_L^0 \rightarrow 3\pi^0$ decay analysis of data. The neutron sample is obtained by scattering neutrons in the beam with an Al plate.	30
6.13	The R_{XY} distribution of the region 2. The red line and arrow indicated the cutoff region	31

List of Tables

2.1	Main K_L^0 decay background modes and their branching ratios	7
4.1	Branching ratio of K_L decays	11
4.2	Summary of the veto cut	12
6.1	Number of events predicted for each source inside the signal region	31

Todo list

Figure: Placeholder: Approval page	i
█ Todo-Fig: Change A B region in different color	xi
█ Present the upper limit at 90% confidence level	xii
█ Add CsI dimension info.	5
█ Put these two sections to the Clustering section	12
█ Need to determine the symbol for the hitXY	19
█ Maybe put this section to the chapter 4 Yield Estimation	23
█ Todo-Fig: Change A B region in different color	25
█ Present the upper limit at 90% confidence level.	27
█ Fig. compare of photon and neutron-like shape	28

¹ Chapter 1

² Introduction

³ 1.1 Motivation

⁴ massless dark photon has not being search, in theoretic study the branching ratio is up to
⁵ 10^{-3} .

⁶ 1.2 Dark Photon

⁷ **Chapter 2**

⁸ **KOTO Experiment**

⁹ **2.1 Introduction**

¹⁰ The KOTO Experiment is a rare decay experiment. The main goal of this experiment is
¹¹ to search for the $K_L \rightarrow \pi^0 \nu \bar{\nu}$ decay. The branching ratio of this decay is predicted to be
¹² $(3.00 \pm 0.30) \times 10^{-11}$ by the Standard Model (SM) [1]. The branching ratio of this decay
¹³ is sensitive to the new physics beyond the SM because of the accuracy. Therefore, the
¹⁴ KOTO experiment is a good place to search for new physics.

¹⁵ **2.2 $K_L \rightarrow \pi^0 \nu \bar{\nu}$**

¹⁶ **2.3 Beam Line**

¹⁷ The KOTO experiment is located at the J-PARC Hadron Experimental Facility (HEF) in
¹⁸ Tokai, Japan.

¹⁹ The HEF is a 30 GeV proton synchrotron. The proton beam has been generated at
²⁰ the end of a linear particle accelerator (LINAC), then into a 3 GeV rapid cycling syn-
²¹ chrotron (RCS), and finally into a 30 GeV synchrotron (MR). At the end extracted from
²² the synchrotron and directed to the Hadron hall. The proton beam is collided with a gold
²³ target and the secondary particles are then directed to the KOTO detector at a 16° to the
²⁴ beamline.

²⁵ **2.4 Detectors**

²⁶ The KOTO detector consists of an electromagnetic calorimeter and other veto counters
²⁷ in a hermetic veto system. The hermetic veto system encloses the decay volume, which
²⁸ supplies a highly evacuated decay region. The veto system contains barrel vetoes, charge
²⁹ vetoes, and other vetoes.

³⁰ **2.4.1 CsI**

³¹ The electromagnetic calorimeter is the main detector of the KOTO experiment. It is used
³² to detect the photon from the K_L decay. The electromagnetic calorimeter consists of 2716
³³ undoped cesium iodide crystals (CsI). The depth of the CsI is 500 mm. The cross-section
³⁴ of crystals has 2 types of units: the small crystal is 25 × 25 mm with 2240 crystals, and the

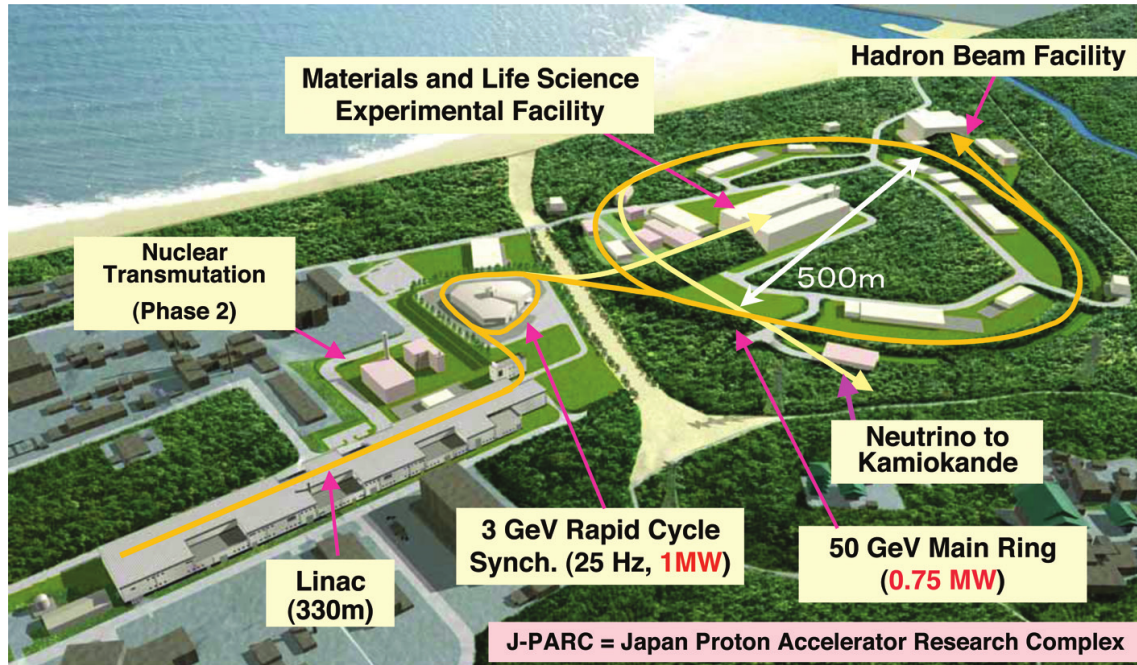


FIGURE 2.1: The entire view of J-PARC. [2]

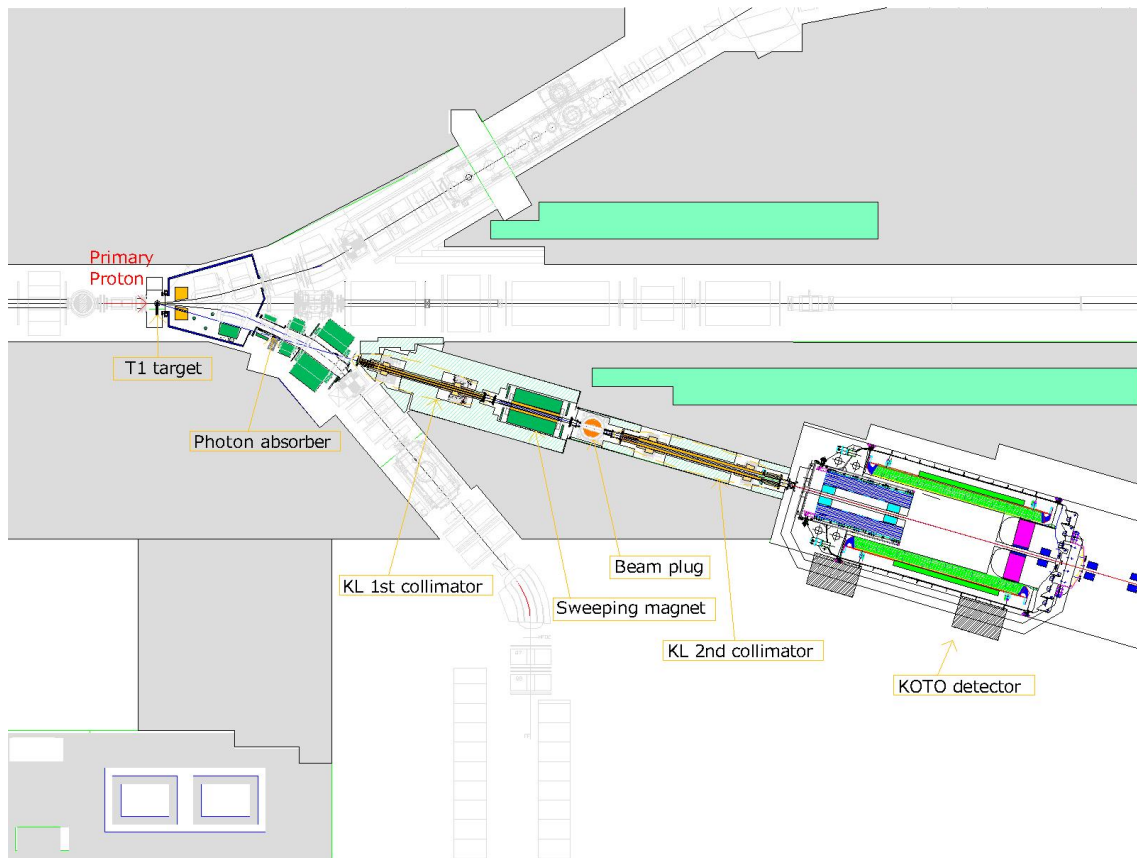


FIGURE 2.2: Beamline layout

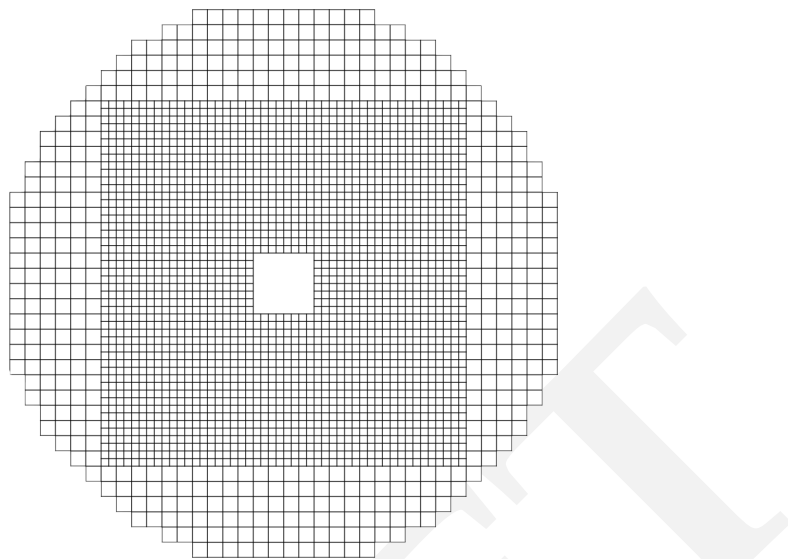


FIGURE 2.3: CsI layout

Add CsI dimension info.

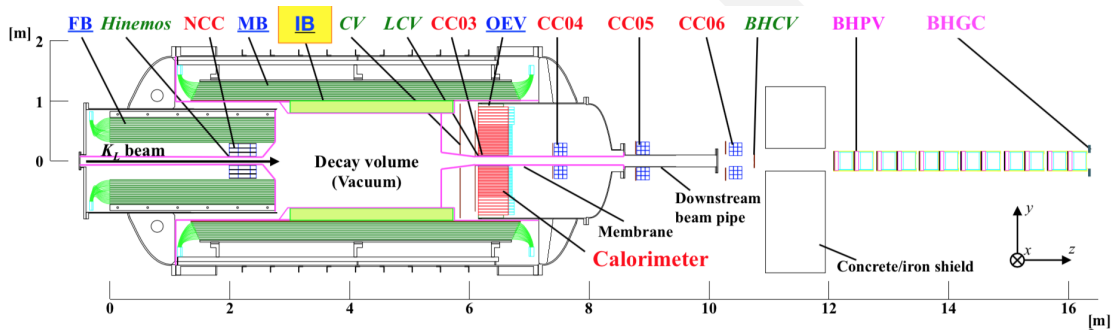


FIGURE 2.4: KOTO detector layout

35 large one is 50×50 mm with 476 crystals. The arrangement of those crystals is shown in
 36 Figure 2.3. The CsI is used to detect the photon from the K_L decay. The CsI is also used to
 37 detect the charged particle from the K_L decay. The CsI is also used to detect the charged
 38 particle from the K_L decay. The CsI is also used to detect the charged particle from the
 39 K_L decay. The small crystal size is smaller than the Molère radius of 35.7 mm. That
 40 allows us to use the shower shape to distinguish the different types of clusters on CsI.
 41 When a photon hits the CsI, the EM shower will be induced and the photon multiplier
 42 tube (PMT) can observe the deposited energy on each crystal. The PMT is connected to
 43 the end of each crystal.

44 In front of the CsI crystal, 4096 Multi-pixel photon counters (MPPC) were glued. This
 45 readout system can be used to measure the shower depth in the calorimeter, by evaluat-
 46 ing the time difference between both ends of the crystal. Which is potentially useful for
 47 discriminating the photon cluster and hadronic-like cluster. Because a hadronic shower
 48 is generally deeper than an EM shower cluster.

49 **2.4.2 Barrel Veto**

50 Barrel veto is the main body of the KOTO detector. It is a veto counter surrounding the
 51 decay volume and is used to detect the photon. There are 3 Barrel Veto Counters in the
 52 KOTO detector, Front Barrel(FB), Main Barrel(MB), and Inner Barrel(IB). As shown in Fig.
 53 [2.4](#), FB covers the upstream region, and MB and IB cover the decay volume. the barrel
 54 veto is divided into 3 layers. The first layer is the innermost layer and is used to detect the
 55 photon. The second layer is the middle layer and is used to detect the charged particle.
 56 The third layer is the outermost layer and is used to detect.

57 **2.4.3 CV**

58 **2.4.4 Other Veto**

59 **2.5 Data Acquisition System**

60 **2.6 Data Taking**

61 **2.7 Trigger**

62 **2.8 Basic Strategy of the Single Cluster Study**

63 **2.8.1 Signal Identification**

64 $K_L^0 \rightarrow \gamma\bar{\gamma}$ decay requires only one photon cluster to hit the CsI calorimeter and without
 65 any in-time hit in the rest of the detector. A single cluster can only provide the energy
 66 and position information. The lack of kinematic constraints will be the challenge of this
 67 study. Moreover, single cluster signatures are easily mimicked by some unknown arbitra-
 68 ry background. Requiring a high photon energy may help to suppress this kind of
 69 background but also reduce the signal efficiency.

70 **2.8.2 Major Background Sources**

71 The major background sources are K_L^0 decay background and neutron-like background.

72 **K_L^0 decay background**

73 Table [2.1](#) shows the main K_L^0 decay backgrounds. Other decay channels are unneces-
 74 sary to be considered because of the low branching ratio. Only $K_L^0 \rightarrow \pi^\pm e^\mp \nu_e$ and
 75 $K_L^0 \rightarrow \pi^\pm \mu^\mp \nu_\mu$ are considered for the decay channel of charged particles in the final
 76 state, due to the high branching ratio. To suppress the K_L^0 decay background, study-
 77 ing these decay channels and understanding their characteristics are important. All of
 78 these decay channels produce more than one photon in the final state. Therefore, it is
 79 easy to suppress these decay channels with the KOTO detector. Except for the decay of
 80 $K_L^0 \rightarrow 2\gamma$, whose final state is similar to the signal signature and may be a potentially
 81 non-eliminable source of background.

TABLE 2.1: Main K_L^0 decay background modes and their branching ratios.

Decay mode	Branching Ratio
$K_L \rightarrow \pi^\pm e^\mp \nu_e$	$(40.55 \pm 0.11)\%$
$K_L \rightarrow \pi^\pm \mu^\mp \nu_\mu$	$(27.04 \pm 0.07)\%$
$K_L \rightarrow 3\pi^0$	$(19.52 \pm 0.12)\%$
$K_L \rightarrow \pi^+ \pi^- \pi^0$	$(12.54 \pm 0.05)\%$
$K_L \rightarrow 2\pi^0$	$(8.64 \pm 0.06) \times 10^{-4}$
$K_L \rightarrow 2\gamma$	$(5.47 \pm 0.04) \times 10^{-4}$

82 **Neutron-like background**

83 The neutron originating from the beamline poses a significant background challenge.
84 Accurately simulating the in-beam neutron background is nearly impossible, especially
85 without a defined mechanism to avoid it. The primary method to mitigate this back-
86 ground involves distinguishing the cluster from the photon event.

⁸⁷ **Chapter 3**

⁸⁸ **Event Reconstruction**

⁸⁹ **3.1 Cluster Finding**

⁹⁰ - CDT

⁹¹ **3.2 Veto Hit Reconstruction**

⁹² - Veto timing - veto hit mechanism – backsplash – fly Backward – upstream decay

⁹³ **3.3 MPPC calibration**

⁹⁴ **3.3.1 Cosmic Ray analysis**

⁹⁵ **3.3.2 T0 correction**

⁹⁶ **3.3.3 $K_L^0 \rightarrow 3\pi^0$ correction**

⁹⁷ **Chapter 4**

⁹⁸ **K_L^0 Yield Estimation**

⁹⁹ The yield of K_L is an important parameter for most analysis in KOTO. To normalize the
¹⁰⁰ Monte Carlo Simulation number of events to the real data, the yield of the $K_L z$ was
¹⁰¹ required. The K_L yield is usually estimated by well-known neutral decay channels with
¹⁰² large branching ratios, which are $K_L^0 \rightarrow 3\pi^0$, $K_L^0 \rightarrow \pi^0\pi^0$, and $K_L^0 \rightarrow 2\gamma$. The branching
¹⁰³ ratio of these three decays is shown in the Table 4.1. The background source of these three
¹⁰⁴ channels is also limited.

TABLE 4.1: Branching ratio of K_L decays

Decay mode	Branching ratio
$K_L^0 \rightarrow 3\pi^0$	$(19.52 \pm 0.12)\%$
$K_L^0 \rightarrow \pi^0\pi^0$	$(8.64 \pm 0.06) \times 10^{-4}$
$K_L^0 \rightarrow 2\gamma$	$(5.47 \pm 0.04) \times 10^{-4}$

¹⁰⁵ The ideal decay channel for the normalization study is $K_L^0 \rightarrow 2\gamma$ decay because the
¹⁰⁶ diphoton final state is relatively similar to the $K_L^0 \rightarrow \gamma\bar{\gamma}$ decay. However, due to insuffi-
¹⁰⁷ cient time for collecting special run data, the statistics of $K_L^0 \rightarrow \pi^0\pi^0$ and $K_L^0 \rightarrow 2\gamma$ decay
¹⁰⁸ are inadequate to estimate the K_L^0 yield. The $K_L^0 \rightarrow 3\pi^0$ decay is a good place to estimate
¹⁰⁹ the K_L yield because its branching ratio is far greater than other neutral decay channels,
¹¹⁰ and a restrictive requirement of the signal signature. Therefore, the $K_L^0 \rightarrow 3\pi^0$ decay was
¹¹¹ accepted to estimate the K_L^0 yield and do the normalization study in this search. If we
¹¹² can get more statistics from the data set, we could do On further study of this search with
¹¹³ better statistics, the normalization study could be based on $K_L^0 \rightarrow 2\gamma$ decay, and use the
¹¹⁴ other two decays to do the cross-check.

¹¹⁵ **4.1 Data Set**

¹¹⁶ The whole special run physics data with the normalization trigger was treated as the data
¹¹⁷ sample. The pre-scaling factor used to scale the number of events collected is set as 13.
¹¹⁸ The control sample uses the Monte Carlo simulation of $K_L^0 \rightarrow 3\pi^0$ including the acciden-
¹¹⁹ tal overlay. Because of the restrictive signal signature of the $K_L^0 \rightarrow 3\pi^0$, the contribution
¹²⁰ of other decay modes can be ignored in the normalization study.

¹²¹ In this study, $1 \times 10^9 K_L^0 \rightarrow 3\pi^0$ decays were prepared for the control sample.

¹²² 4.2 Event Selections

¹²³ In the K_L^0 Yield study, the event selection aims to purify the $K_L^0 \rightarrow 3\pi^0$ decay events and
¹²⁴ reject corresponding background events. The event selection consists of the veto cut and
¹²⁵ kinematic cut.

¹²⁶ 4.2.1 Veto Cut

¹²⁷ The veto cut is a simple criterion of an in-time hit in the veto counter. All the veto cuts
¹²⁸ applied to the yield study are the same as the veto cuts used in the $K_L^0 \rightarrow \pi^0\nu\bar{\nu}$ analysis[3].
¹²⁹ The summary of the veto cut is shown in Table 4.2.

TABLE 4.2: Summary of the veto cut

Veto Counter	Energy Threshold	Timing Window
FB	1 MeV	51ns
NCC and HINEMOS	1 MeV	40ns
MB	1 MeV	20ns
IB	1 MeV	20ns
MBCV	0.5 MeV	60ns
IBCV	0.5 MeV	60ns
CV	0.2 MeV	20ns
LCV	0.6 MeV	30ns
CSI (isolated crystal)	see Sec. 4.2.1	20ns
CSI (extra cluster)	see Sec. 4.2.1	20ns
OEV	1 MeV	20ns
CC03	3 MeV	30ns
CC04, CC05, CC06 (CSI crystal)	3 MeV	30ns
CC04, CC05, CC06 (plastic scintillator)	1 MeV	30ns
BPCV	1 MeV	24ns
BHCV ¹	221 eV	25ns
BHPV ²	2.5 p.e.	15ns
BHGC ³	2.5 p.e.	15ns

¹ BHCV requires hits in more than two modules.

² BHPV requires hits in more than three consecutive modules.

³ BHGC veto accepts the number of equivalent photons instead of energy.

Put these two sections to the Clustering section

¹³⁰ In the following section, a detailed explanation of the some Veto Cut is shown.

¹³² Isolated Crystal Veto

¹³³ An isolated crystal hit very close in time to the photon clusters are possibly comes from
¹³⁴ the same K_L^0 decay. To reject this kind of background, a timing window of ± 10 ns of the

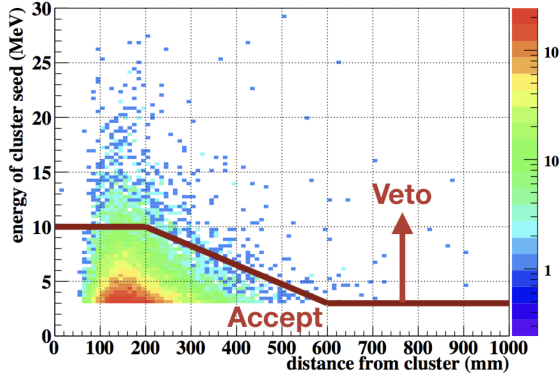


FIGURE 4.1: Distribution of isolated crystal hit energy(E) vs. its distance(D) from the nearest cluster. The red line shows the cut based on Equation 4.1. The sample was obtained from the $K_L^0 \rightarrow \pi^0\nu\bar{\nu}$ Monte Carlo simulation. Figure courtesy of [4]

¹³⁵ nearest photon cluster timing is required in this veto. A multistep cut based on the hit
¹³⁶ Energy(E) and Distance(D) from the closest cluster is applied, as the following equation:

$$\begin{cases} E > 10 \text{ [MeV]} & , \text{if } D < 200 \text{ [mm]} \\ E > 10 - \frac{7(D-200)}{400} \text{ [MeV]} & , \text{if } 200 \leq D \leq 600 \text{ [mm]} \\ E > 3 \text{ [MeV]} & , \text{if } D > 600 \text{ [mm]} \end{cases} \quad (4.1)$$

¹³⁷ As shown in Figure 4.1, a higher energy threshold is required for the isolated crystal
¹³⁸ to hit nearer to the cluster, to bypass the shower propagation effect.

¹³⁹ Extra Cluster Veto

¹⁴⁰ A cluster hit in the CsI calorimeter that is not associated with the π^0 decay is considered
¹⁴¹ an extra cluster. If the timing of the extra cluster is within ± 10 ns of the reconstructed π^0
¹⁴² vertex time, it is considered as a background and rejected.

¹⁴³ 4.2.2 Kinematic Cut

¹⁴⁴ The kinematic cut is based on the photon information and the reconstructed physics
¹⁴⁵ quantities of K_L^0 and π^0 . A detailed explanation of the kinematic cut is shown in the
¹⁴⁶ following section.

- 147 **Trigger timing**
 148 **Total Energy in CsI**
 149 **Photon Energy**
 150 **Photon Hit Position**
 151 **Minimum Cluster Distance**
 152 χ_z^2
 153 ΔT_{vtx}
 154 K_L^0 Vertex Z (Z_{vtx})
 155 K_L^0 Mass
 156 $K_L^0 P_T$
 157 π^0 Mass
 158 $K_L^0 \Delta Z$

159 4.3 Yield Estimation

160 The Yield of the K_L^0 (Y) in the data set is defined by the following equation:

$$161 Y = \frac{N_{mode}}{\mathcal{BR}_{mode} \times A_{mode}} \quad (4.2)$$

162 where N_{mode} is the number of events, \mathcal{BR}_{mode} is the branching ratio, and A_{mode} is the
 163 acceptance. The mode could be any decay channel of the K_L^0 . The acceptance(A_{mode}) can
 be evaluated by the Monte Carlo simulation, as the following equation:

$$164 A_{mode} = \frac{N_{remaind}}{N_{gen}} \quad (4.3)$$

165 where $N_{remaind}$ is the number of events that pass the event selection, and N_{gen} is the
 166 number of generated K_L^0 decays. And because the K_L^0 yield is proportional to the number
 167 of protons on target (POT), the K_L^0 flux (F) can be defined as the yield per POT, as shown
 in the following equation:

$$168 F = \frac{Y}{POT} \quad (4.4)$$

169 As mentioned in Section 4.1, the normalization trigger was used to be the data sample.
 170 Because the normalization trigger was taken simultaneously with the physics trigger, the
 171 K_L^0 yield is the same as the physics trigger. Therefore, the K_L^0 yield evaluated by the
 normalization trigger can be used directly in the physics analysis.

172 In this study, the K_L^0 yield was estimated by the $K_L^0 \rightarrow 3\pi^0$ decay. All the kinematic
 173 cuts introduced in Section 4.2.2 and the veto cuts summarized in Table 4.2 were imposed.

174 4.3.1 Estimation by $K_L^0 \rightarrow 3\pi^0$ Decays

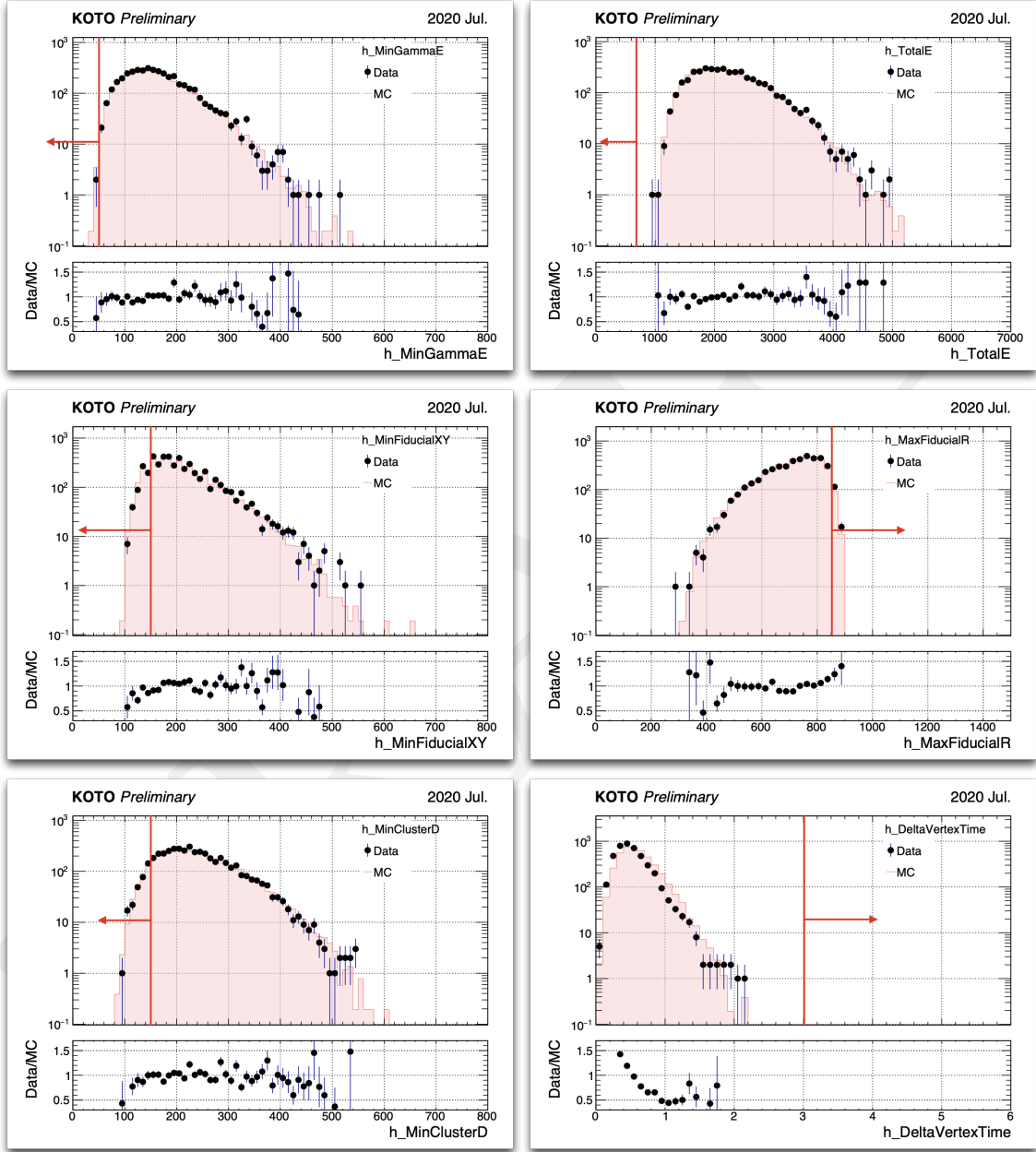


FIGURE 4.2: Distribution of the kinematic variables for the $K_L^0 \rightarrow 3\pi^0$ decay. All the selections are applied except the variable shown in the plot. The black point shows the data, and the fill histogram shows the Monte Carlo simulation. The red arrow indicates the cut-off value of the variable.

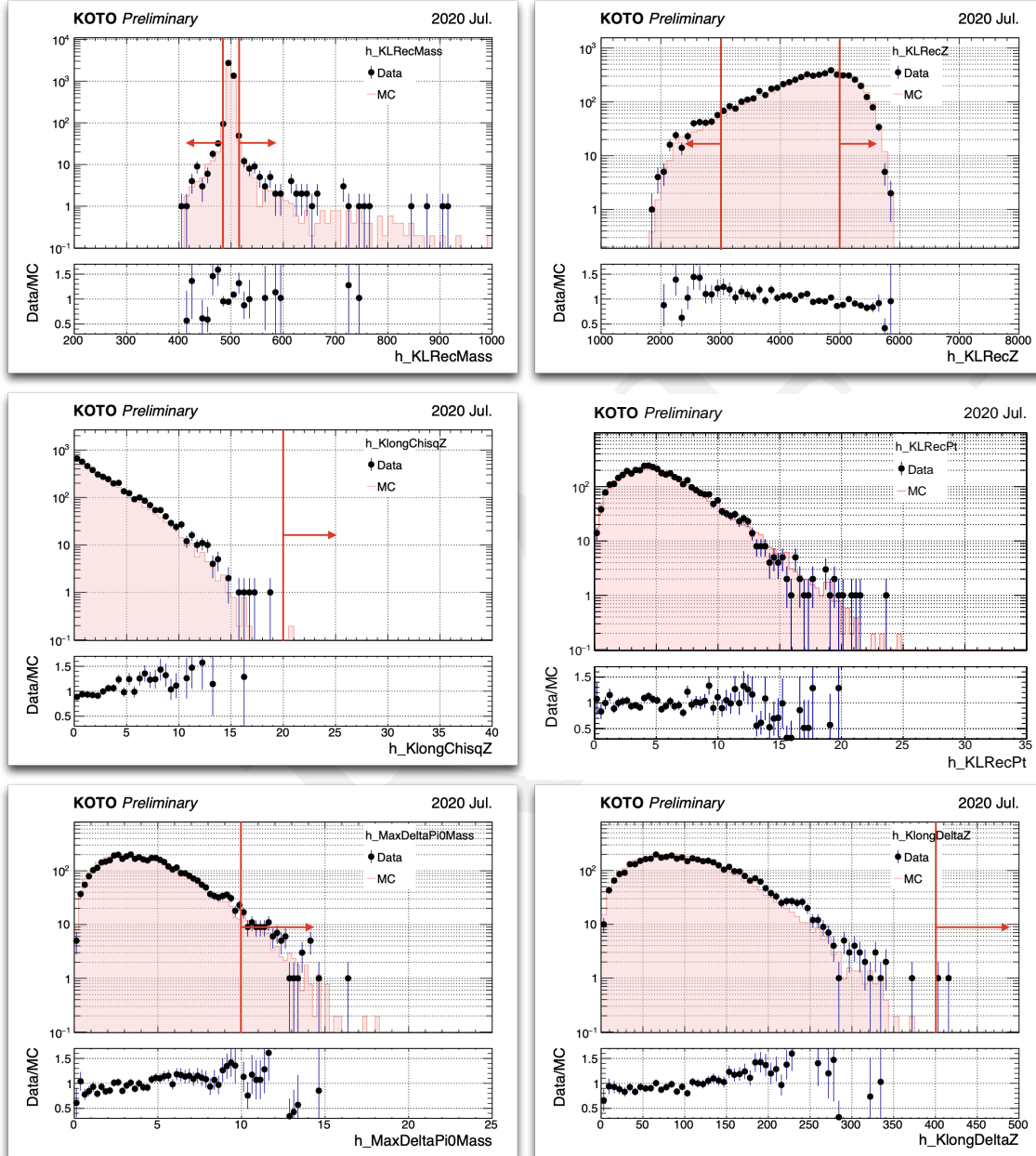


FIGURE 4.3: Distribution of the kinematic variables for the $K_L^0 \rightarrow 3\pi^0$ decay. All the selections are applied except the variable shown in the plot. The black point shows the data, and the fill histogram shows the Monte Carlo simulation. The red arrow indicates the cut-off value of the variable.

¹⁷⁵ **Chapter 5**

¹⁷⁶ **Monte Carlo Simulation**

¹⁷⁷ **5.1 GEANT4**

¹⁷⁸ **5.2 Accidental Overlay**

¹⁷⁹ **5.3 Beamline simulation**

¹⁸⁰ **5.4 Other Simulations**

¹⁸¹ **5.4.1 NCC background**

¹⁸² **5.4.2 Halo Kaon**

¹⁸³ **5.4.3 Charge Kaon**

¹⁸⁴ **Chapter 6**

¹⁸⁵ **Analysis of $K_L \rightarrow \gamma\bar{\gamma}$**

¹⁸⁶ The goal of the $K_L^0 \rightarrow \gamma\bar{\gamma}$ analysis is to estimate the branching ratio (\mathcal{BR}) of this decay,
¹⁸⁷ we took a 2-hour special run with a single cluster trigger in 2020. The distinctive signal
¹⁸⁸ signature of $K_L^0 \rightarrow \gamma\bar{\gamma}$ manifests as a singular photon hit on the CsI calorimeter, devoid
¹⁸⁹ of any in-time hits on other detectors.

¹⁹⁰ Employing a blind analysis method, we define a specific region, characterized by en-
¹⁹¹ ergy deposition $800 \text{ MeV} < E_\gamma < 3000 \text{ MeV}$ and a spatial constraint of $300 \text{ mm} < R_{XY}$
¹⁹² $< 850 \text{ mm}$, where R_{XY} denotes the maximum distance between the hit location and the
¹⁹³ center of the CsI crystal along the x and y axes. The signal region has to be within the
¹⁹⁴ blind region and has been optimized.

¹⁹⁵ Need to determine the symbol for the hitXY

¹⁹⁶ Our principal objective revolves around suppressing background noise and accentu-
¹⁹⁷ ating signal events through event selection. Subsequently, we estimate the residual back-
¹⁹⁸ ground events within the signal region post-selection. Under the assumption of negli-
¹⁹⁹ gible background noise, we calculate the Single Event Sensitivity (SES) to estimate the
²⁰⁰ branching ratio upon observing signal events within the defined signal region. The SES,
²⁰¹ representing the reciprocal of the product of the total K_L^0 yield and the acceptance of
²⁰² signal decays, is expressed mathematically as:

$$SES = \frac{1}{Y \times A_{sig}} \quad (6.1)$$

²⁰³ Here, Y represents the K_L^0 yield, and A_{sig} signifies the signal acceptance. The branching
²⁰⁴ ratio (\mathcal{BR}) is then inferred from SES and the observed number of signal events (N_{sig})
²⁰⁵ within the signal region, as articulated by:

$$\mathcal{BR} = SES \times N_{sig} \quad (6.2)$$

²⁰⁶ However, when background contributions cannot be negligible, a statistical methodol-
²⁰⁷ ogy becomes imperative to ascertain the upper and lower bounds of signal event counts.
²⁰⁸ The background level (N_{bg}) is estimated through two approaches in this study. For K_L
²⁰⁹ decay backgrounds, Monte Carlo simulations are employed to evaluate N_{bg} , defined by:

$$N_{bg} = Y \times \mathcal{BR}_{bg} \times A_{bg} \quad (6.3)$$

210 Were \mathcal{BR}_{bg} represents the branching ratio of specific background decays (e.g., $K_L \rightarrow 2\gamma$),
 211 and A_{bg} denotes the acceptance corresponding to this background decay. For neutron
 212 backgrounds, a dedicated neutron data run is utilized, employing a data-driven approach
 213 for background-level evaluation through normalization against the neutron-dominant
 214 region between physics data and neutron data sample. Upon combining all background
 215 sources, a prediction of the background level within the signal region is determined. Af-
 216 ter an examination of reliability through the side-band region, uncover the blind region.

217 This chapter unfolds with a presentation of the event selection criteria, followed by
 218 a discussion on background suppression methodologies. Subsequently, the reliability
 219 of our analysis is assessed through a comparison between physics data and simulation
 220 results in the side-band region. The computation of background levels and SES is then
 221 detailed. With the final estimation in hand, we will proceed to open the box and the
 222 interpretation of the statistical result will be presented at the latest.

223 6.1 Event Selection

224 The event selection included trigger cuts, kinematic cuts, and veto cuts. The trigger cuts
 225 were designed to mimic the online trigger effect, while the kinematic cuts and veto cuts
 226 were implemented to suppress background noise. The kinematic cuts were based on the
 227 reconstruction quantities of the photon cluster, while the veto cuts were just the criteria
 228 of hit on the veto counters. In the single cluster study, the signal significance of $K_L \rightarrow \gamma\bar{\gamma}$
 229 is only one photon cluster hit on the CsI calorimeter. And other vetoes keep silent in
 230 time. Which means a very loose condition for hitting events. It is also a challenge for this
 231 study.

232 6.1.1 Trigger Selection

233 The online trigger effect is the source of the difference between the collected data and the
 234 Monte Carlo simulation. To mimic the online trigger effect and ensure the consistency of
 235 the data and MC simulation, two trigger selections were implemented: the trigger timing
 236 cut and the total energy cut.

- 237 • **Timing window**

238 The online trigger will reject all events with any on-time veto hit, thus a trigger
 239 timing window as shown in Figure 6.1 is required to eliminate the online trigger
 240 effect. In the real data taking, due to the 8-ns clock dead time, the real physics data
 241 timing distribution will be wider than the Monte Carlo simulation. A wide enough
 242 timing window is selected to cover the distribution inconsistency between the data
 243 and the MC simulation.

- 244 • **Total Energy**

245 The offline energy cut should be larger than the online ET threshold to eliminate the
 246 online ET trigger effect. The online ET threshold of 300 MeV was required in the

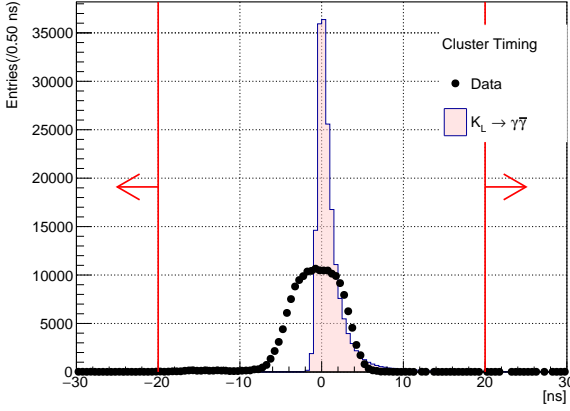


FIGURE 6.1: Distribution of cluster timing after relative timing correction. The dot is from real physics data, and the filled histogram is the MC simulation. The red arrow is the cut-off region.

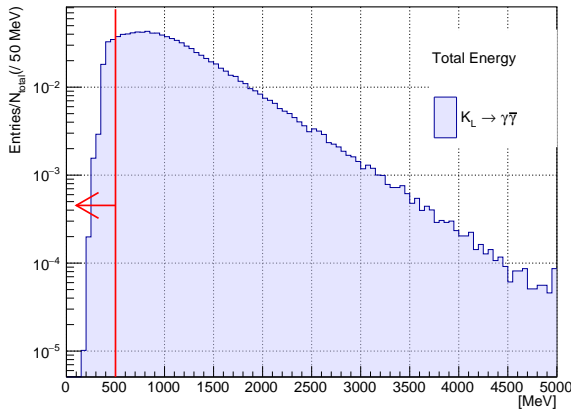


FIGURE 6.2: Distribution of total energy from Monte Carlo simulation. The histogram area is normalized to 1. The red arrow is the cut-off region.

247 special run, Thus, the offline energy cut is set as 500 MeV. As shown in the Figure
 248 6.2, the signal acceptance is 91.0%

249 6.1.2 Kinematic Cuts

250 The $K_L \rightarrow \gamma\bar{\gamma}$ decays require only one photon cluster on the CsI calorimeter. Therefore,
 251 the reconstruction of the mother particle is not possible, and also some variables based
 252 on multiple photon clusters will be absent, such as the vertex position, cluster distance,
 253 and KL kinematic quantities. As kinematic constraints are lacking, kinematic selection is
 254 determined by only two variables: the photon hit position and photon energy.

- 255 • **Innermost and Outermost Photon Hit Position**

256 To prevent the edge of the calorimeter from affecting cluster reconstruction, any
 257 event that hits the boundary will be removed. Based on the geometry of the calorimeter,
 258 the outer boundary is evaluated using radius of hit position, R_γ , while the inner
 259 boundary is evaluated using the maximum of the absolute values of x and y of the
 260 photon hit position, $\max\{|x_\gamma|, |y_\gamma|\}$. The inner boundary is set as a $300 \times 300 \text{ mm}^2$
 261 box, while the outer boundary is a circle with a radius of 850 mm, as shown in
 262 Figure 6.3.

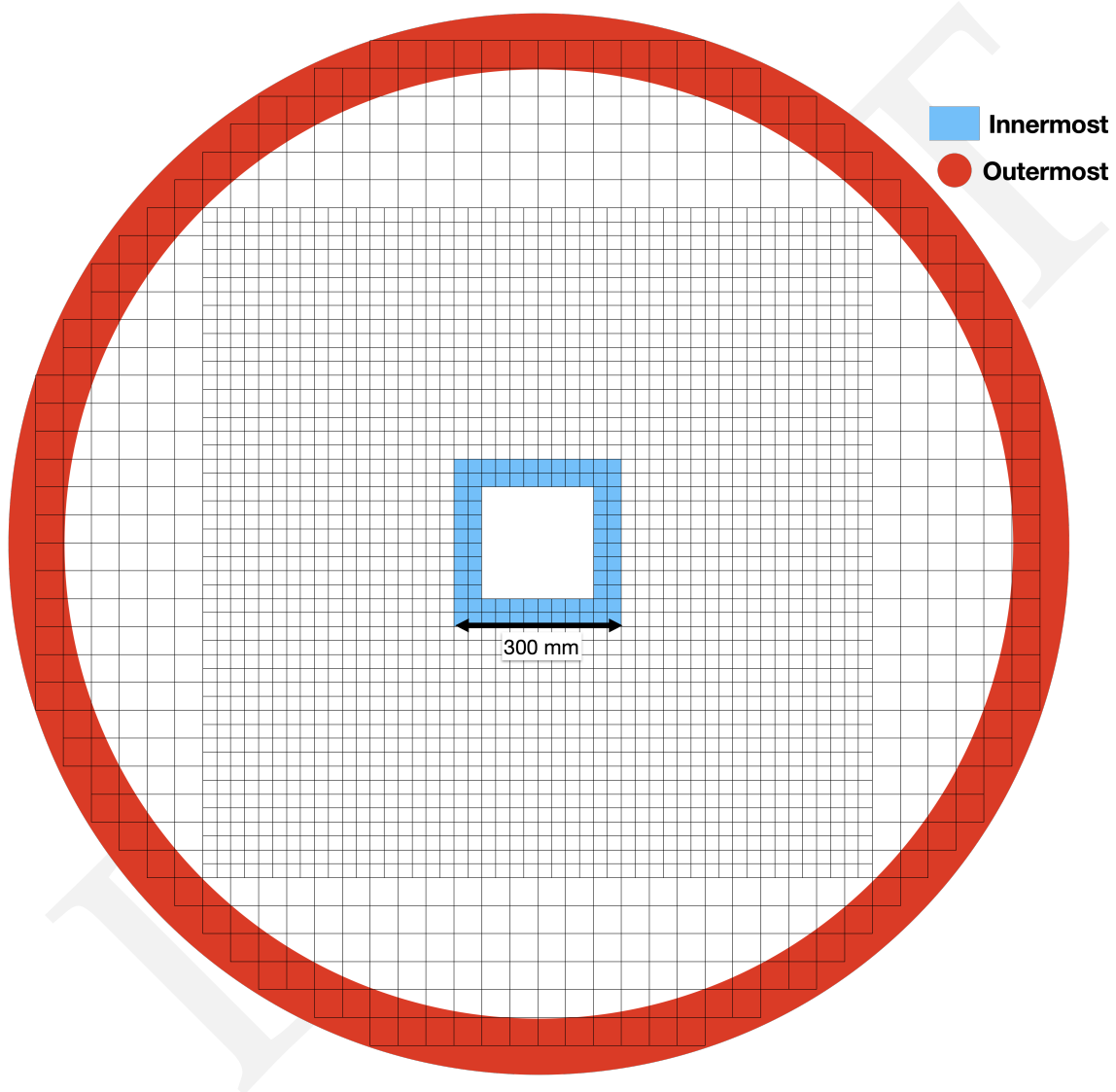


FIGURE 6.3: An upstream view of the CsI calorimeter. The red region is the outermost boundary, while the blue region is the innermost boundary.

263 • **Photon energy**

264 Because of the 1 cluster study, the photon energy is almost equivalent to the total
 265 energy. Therefore, simply required photon energy to be larger than 500 MeV, which
 266 is the same as the total energy cut.

267 **6.1.3 Veto Cuts**

268 Maybe put this section to the chapter 4 Yield Estimation

269 Veto counters are the primary tool for Kaon decay background suppression in the
 270 KOTO experiment. The veto hits within the veto timing window and above the veto
 271 energy threshold will be tagged as an in-time veto hit. The event with any in-time veto
 272 hits will be treated as a background event and rejected. In the following veto cuts study,
 273 the determined method of the veto timing window and the veto energy threshold will be
 274 discussed.

275 **FBAR and NCC**

276 • **Upstream decays**

277 (K_L^0 decays inside the FBAR.)

278 • **Backward hit**

279 (K_L^0 decays inside MB and flies backward to hit FBAR or NCC.)

280 • **CsI backsplash**

281 ()

282 **MB and IB**

283 **CV**

284 **Others**

285 (Other Veto counters, CC03, CC04, CC05, CC06, OEV, IBCV, MBCV, BHPV and BHGC.)

286 **6.2 Background Suppression**

287 There are two main category background sources in this analysis: K_L decay events and
 288 Hadronic cluster. Besides these two main background sources, we will also discuss the
 289 other background sources that we study in this analysis, such as Charge Kaon decays,
 290 NCC background, and Halo Kaon backgrounds. In the following section, we will talk
 291 about the background suppression strategy for each category.

292 **6.2.1 K_L Decay Background**

293 In this analysis, we have studied the major three K_L^0 neutral decay channels, like $K_L^0 \rightarrow$
 294 $3\pi^0$, $K_L^0 \rightarrow \pi^0\pi^0$, and $K_L^0 \rightarrow 2\gamma$. And also the K_{e3}^0 , $K_{\mu 3}^0$, and $K_L^0 \rightarrow \pi^+\pi^-\pi^0$, which is the
 295 charge decay channel with a large branching ratio.

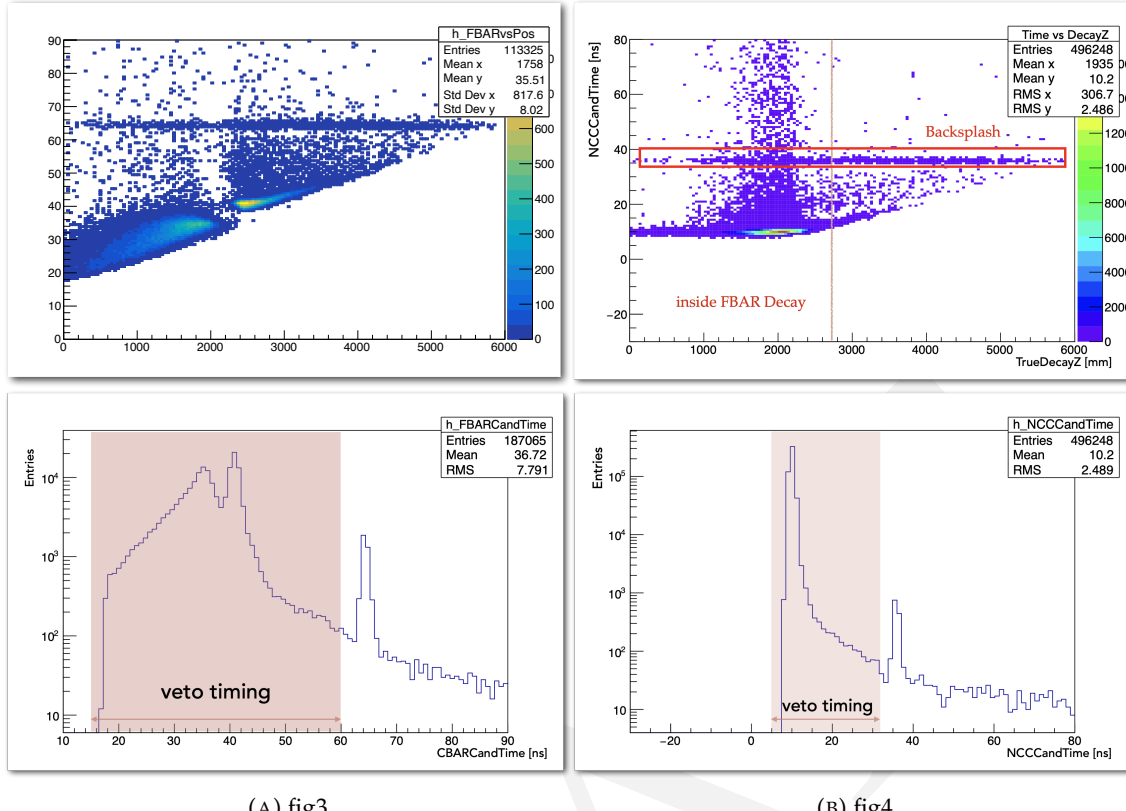


FIGURE 6.4: Temporary plots of FBAR and NCC

There are 3 kinds of possible mechanisms from K_L^0 decays were found:

- **Missing photon**

One photon hits the CsI, but other particles hit the dead material of the KOTO detector or missing in the beam hole.

- **Upstream decay**

K_L^0 decay upstream of the FBAR, one photon hits the CsI, and the other photon missing outside the detector.

- **Fusion cluster**

The decay position along the Z-axis (Z_{vtx}) is too close to the CsI, all decay products hit the nearby crystal and are noted as a single cluster by the clustering process. As shown in Figure 6.7

In this section, all the studied K_L^0 backgrounds will be discussed. All the Monte Carlo simulations were applied the accidental overlay.

309 $K_L^0 \rightarrow 2\gamma$ Background

310 Because of the extreme hermetic of the KOTO detector, the possibility of missing multiple
311 particles is very low. And with our powerful charge veto counter, it is also very difficult

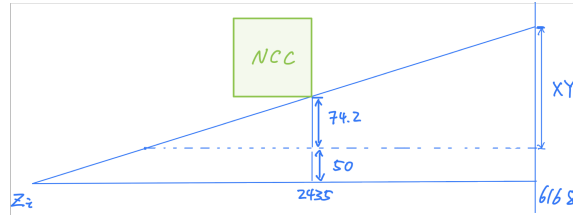


FIGURE 6.5: The schematic geometry diagram of the mechanism of the upstream decay background.

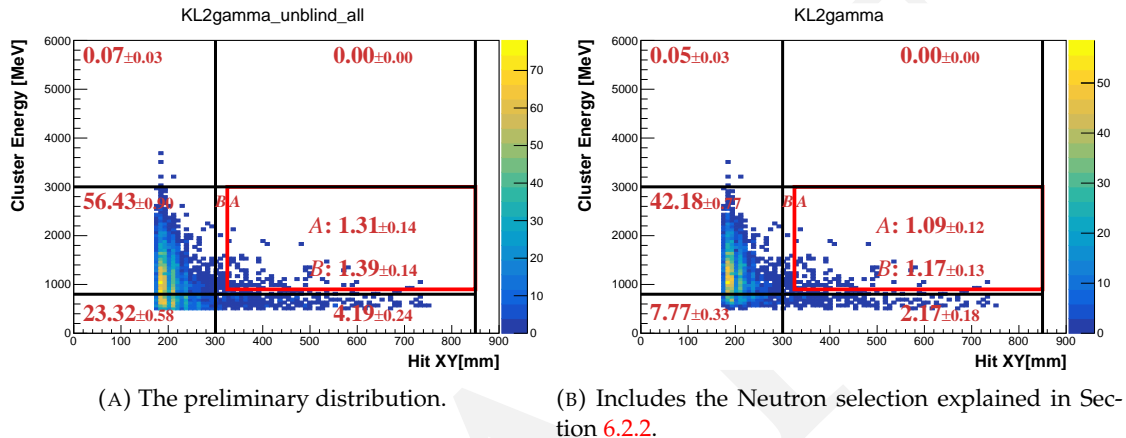


FIGURE 6.6:

Todo-Fig: Change A B region in different color

$E_\gamma - R_{XY}$ distributions of scattered $K_L^0 \rightarrow 2\gamma$ decays with various cut. The red frame indicates the signal region. The red number indicates the background level in each region.

312 to miss a charged particle. Therefore, $K_L^0 \rightarrow 2\gamma$ decay with one missing photon will be
313 the primary K_L^0 decay background in this study.

314 $K_L^0 \rightarrow 2\gamma$ background consists of two mechanisms, missing photon and upstream de-
315 cay. $K_L^0 \rightarrow 2\gamma$ has very similar signature with the $K_L^0 \rightarrow \gamma\bar{\gamma}$, the only difference is another
316 photon is visible. This means if the other photon of $K_L^0 \rightarrow 2\gamma$ is missing detecting, this
317 event will be an ineliminable background in this study. The upstream decay mechanism
318 is also having a missing photon. But its decay position is upstream of the FBAR, which
319 highly constrains the hit radius (R_{XY}) of the cluster. Based on the geometry calculation
320 as shown in Figure 6.5, the maximum R_{XY} of the cluster of upstream decay is 265 mm,
321 which is outside the signal region.

322 Figure 6.6 shows the result of K_L^0 selection. A background level of 1.09 ± 0.12 is es-
323 timated in the signal region.

324 Other K_L^0 decay Backgrounds

325 Besides the $K_L^0 \rightarrow 2\gamma$ background, the other K_L^0 decay backgrounds are also studied in
326 this analysis. Such as $K_L^0 \rightarrow 3\pi^0$, $K_L^0 \rightarrow \pi^0\pi^0$, K_{e3}^0 , $K_{\mu 3}^0$ and $K_L^0 \rightarrow \pi^+\pi^-\pi^0$. After the
327 event selection explained in Section 6.1 and 6.2.2, the event inside the signal region of all

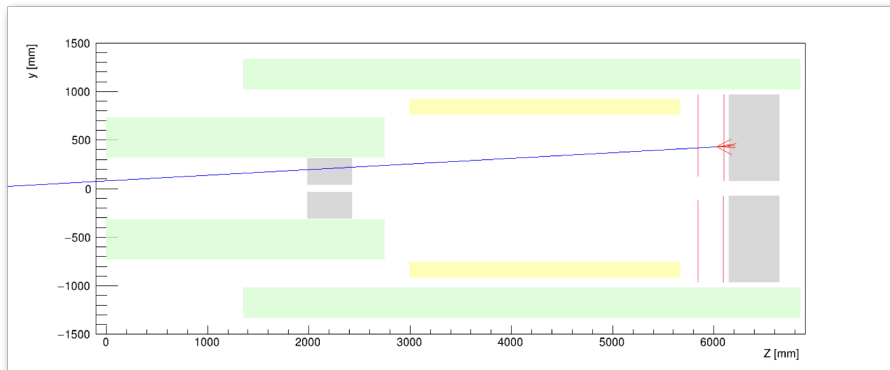


FIGURE 6.7: The schematic geometry diagram of the mechanism of the fusion cluster background.

328 decays except $K_L^0 \rightarrow 2\gamma$ is all rejected. All the three mechanisms mentioned above existed
 329 in these decays. The missing photon is also an ineliminable background, but because the
 330 decay products are much more than the $K_L^0 \rightarrow 2\gamma$, the missing photon background is
 331 negligible. And the upstream decay background has the same geometry constraint as the
 332 $K_L^0 \rightarrow 2\gamma$.

333 The fusion cluster mechanism is the most challenging one because the usual method
 334 to reject this kind of background is to restrict the decay vertex Z (Z_{vtx}) position in a
 335 reasonable region. However, in this study, the Z_{vtx} is not available due to the lack of
 336 kinematic variables. Therefore, we have to distinguish the fusion cluster from the single
 337 cluster by the cluster shape.

338 The fusion cluster will have a wider shape than the single cluster because the fusion
 339 cluster is the combination of two clusters. Which is more likely to be a hadronic-like clus-
 340 ter. Thus, cluster shape discrimination with deep learning (CSDDL), which is explained
 341 in Section 6.2.2, is sensitive to distinguish the fusion cluster from the single cluster.

342 If we assume the BR to be $\mathcal{O}(10^{-3})$, the number of signal events inside the signal region
 343 is $\mathcal{O}(10^5)$. That means the Kaon decay background is negligible in this study.

344 Figure 6.8 shows the background level of other K_L^0 decays. The upper limit at 90%
 345 confidence level is estimated in the signal region, as shown in Table 6.1.

346 6.2.2 Hadronic Background

347 Neutron cluster background is the dominant background in this study. The mechanism
 348 is that a neutron enters the calorimeter with only one cluster hit, as illustrated in Figure
 349 ???. We have three tools to suppress the neutron background: cluster shape discrimina-
 350 tion with deep learning (CSDDL), pulse shape discrimination by using Fourier analysis
 351 (FPSD), and a shower depth measurement.

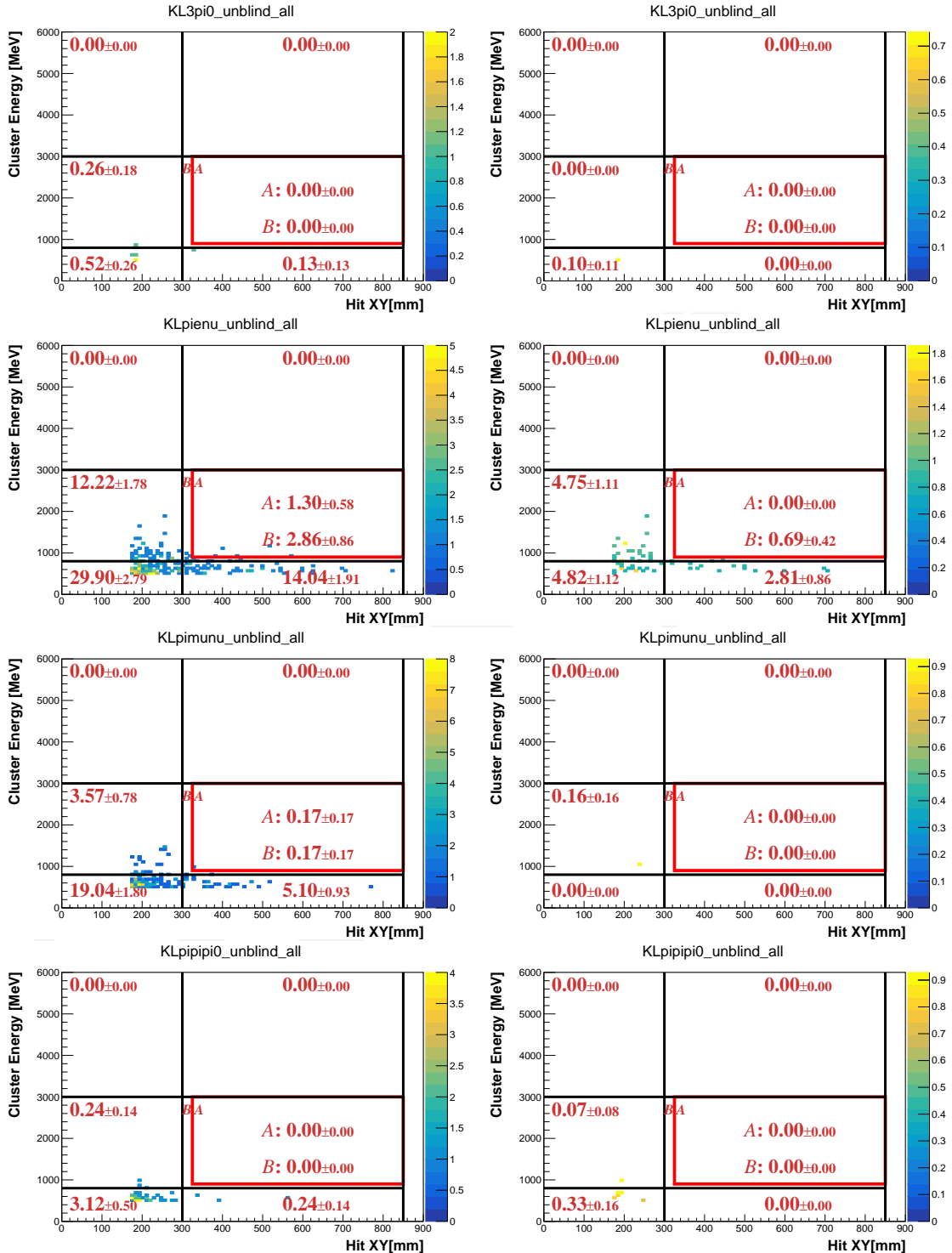


FIGURE 6.8:

Present the upper limit at 90% confidence level.

$E_\gamma - R_{XY}$ distributions of various background sources after applying all selection cuts. Left-hand side plots exclude the neutron cuts and the right-hand side plots include it. The red frame indicates the signal region. The red number indicates the background level in each region.

352 **Cluster Shape Discrimination with Deep Learning(CSDDL)**

353 The cluster shape of hadronic-like events is different from the photon-like events. Be-
 354 cause of the shower depth, the neutron-like event will be wider and shallower, the photon-
 355 like event will look narrow and depth.

356 Fig. compare of photon and neutron-like shape

357 Therefore, we can discriminate each other by cluster shape. However, this discrimina-
 358 tion work is a heavy workload, we use a deep learning model to help us quickly do the
 359 jobs. This model is based on the Convolutional Neural Network (CNN) architecture[5].
 360 The input of the training is the energy and timing of each crystal of the cluster. And the
 361 cluster energy and hit angle (θ).

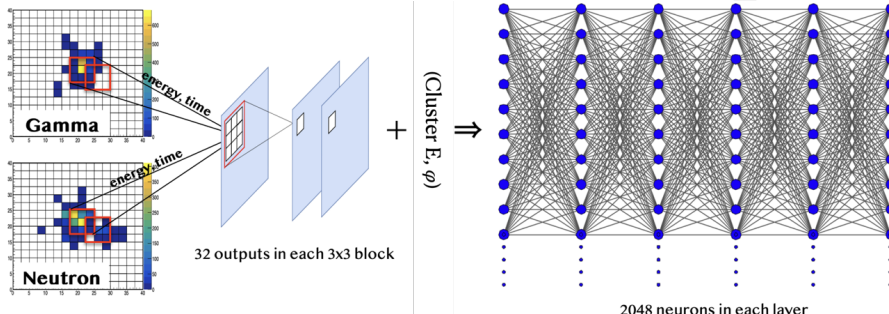


FIGURE 6.9: The architecture of CSD neural network training process.

362 **Fourier transforms for Pulse shape discrimination (FPSD)**

363 The difference in shower development also manifests in the pulse shape difference. FPSD
 364 discriminated the neutron cluster and photon clusters based on the shape of the ADC
 365 waveform. We applied FTT to the ADC raw pulse and then extracted the differences be-
 366 tween the neutron and photon in the frequency domain. Figure 6.10 shows the likelihood
 367 ratio. By requiring the 90% signal acceptance, the neutron cluster background rejection
 368 efficiency is 89.6%.

369 **Shower-depth**

370 The radiation length for photons is shorter than the interaction length for neutrons, re-
 371 sulting in different shower depths in the calorimeter for photons and neutrons. Multi-
 372 pixel photon counters (MPPC) were installed in front of the CSI calorimeter, to get the
 373 timing difference(ΔT) between PMT and MPPC as shown in figure 6.11. The distribution
 374 of ΔT is shown in figure 6.12. By requiring ΔT to be less than 29.5 ns, the background
 375 rejection efficiency is 84% with a signal loss of 9%.

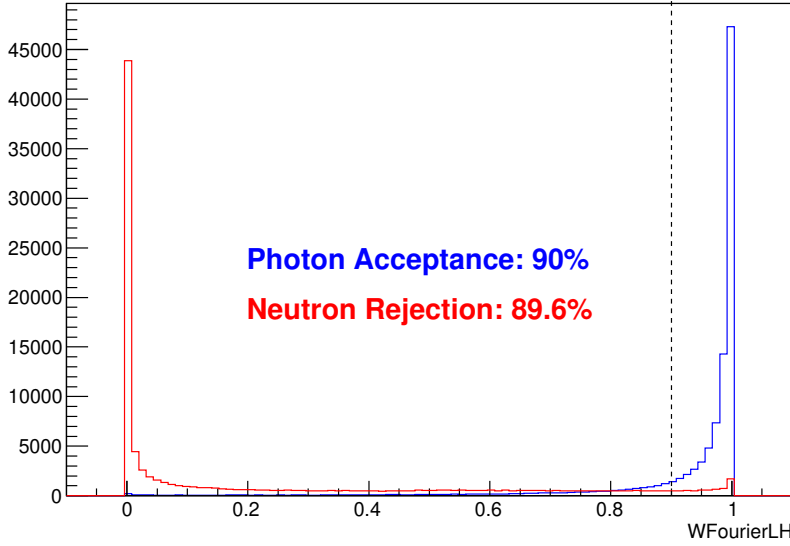


FIGURE 6.10: Distribution of the likelihood ratio for hadronic cluster events (red) and photon cluster events (blue). The photon cluster events are obtained through the $K_L^0 \rightarrow 3\pi^0$ decay analysis of data. The neutron sample is obtained from neutron data.

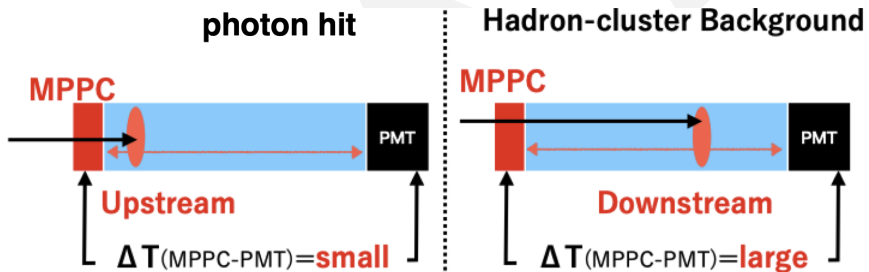


FIGURE 6.11: Illustration of shower depth means. An MPPC is installed on the upstream side. The time difference between the photon arriving upstream and downstream ($\Delta T = T_{MPPC} - T_{PMT}$) is used to measure the depth of the reaction and distinguish between photon events (left) and neutron events (right).

376 6.2.3 Low Radius Event background

377 After the event selection, there is a large discrepancy between the data and the simula-
 378 tion in the low-radius region. As shown in Figure 6.13, the data has a higher level of
 379 background in the low-radius region than the simulation. To figure out the contribution
 380 of this discrepancy, we studied the following background sources.

381 Upstream Decay from 2nd Collimator

382 The discrepancy is centered at the region $R_{XY} < 175$ mm and the maximum R_{XY} of the
 383 cluster of upstream decay is 265 mm, as Section 6.2.1 discussed. This means the upstream
 384 decay is a very possible background source. Therefore, we extend the generated position
 385 in the Monte Carlo simulation to the start of the 2nd collimator to study the very up-
 386 stream decay background. In the usual simulation, the decay position is generated at

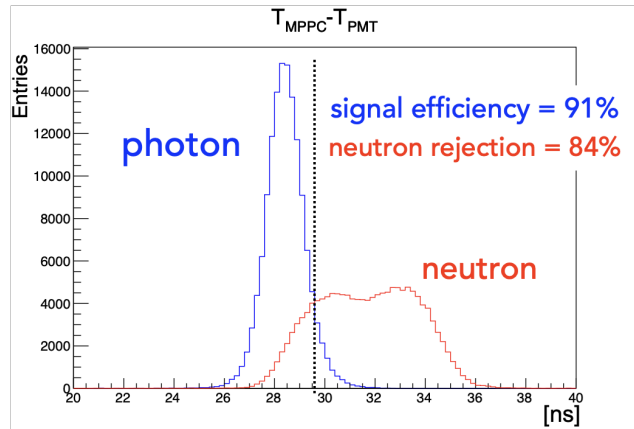


FIGURE 6.12: Distribution of the ΔT for neutron events and photon events. The photon cluster events are obtained through the $K_L^0 \rightarrow 3\pi^0$ decay analysis of data. The neutron sample is obtained by scattering neutrons in the beam with an Al plate.

387 the end of the 2nd collimator, which is -1507 mm from the upstream of the FBAR. The
 388 2nd collimator is 4 m long, which means the new decay position is -5507 mm from the
 389 upstream of the FBAR. The geometry calculation, as Figure 6.5, shows that the maximum
 390 R_{XY} of the cluster of the new decay position is 133 mm, which completely covers the
 391 discrepancy region.

392 The $K_L^0 \rightarrow 2\gamma$ decay was studied in this section. The normalization method is the
 393 same as the usual Monte Carlo simulation but uses the upstream $K_L^0 \rightarrow 3\pi^0$ decay ($Z=-$
 394 5507 mm) to estimate the K_L^0 yield.

395 **Upstream π^0 background**

396 **Charge Kaon Decay**

397 **Halo Kaon Background**

398 6.3 Single Event Sensitivity

399 After considering the 175 mm cut for the low-radius background and all the selection
 400 cuts, the single event sensitivity (SES) is calculated by the equation 6.1. The SES is calcu-
 401 lated by the K_L^0 yield and the signal acceptance. For this study, The K_L^0 yield is evaluated
 402 by the $K_L^0 \rightarrow 3\pi^0$ decay, because the statistics of the 2-hour special physics data set are
 403 not enough to evaluate the yield by $K_L^0 \rightarrow \pi^0\pi^0$ and $K_L^0 \rightarrow 2\gamma$ decays. After the selection
 404 cuts in Section ??, no event will leave for the $K_L^0 \rightarrow \pi^0\pi^0$ and $K_L^0 \rightarrow 2\gamma$ decays. The
 405 signal acceptance is evaluated by the Monte Carlo simulation with accidental overlay.
 406 After applying all the selection cuts in Section 6.1, the signal acceptance is 2.66×10^{-3} .
 407 And the K_L^0 yield is 1.29×10^{10} . The single event sensitivity (SES) is estimated to be
 408 $(2.91 \pm 0.05_{\text{stat.}}) \times 10^{-8}$.

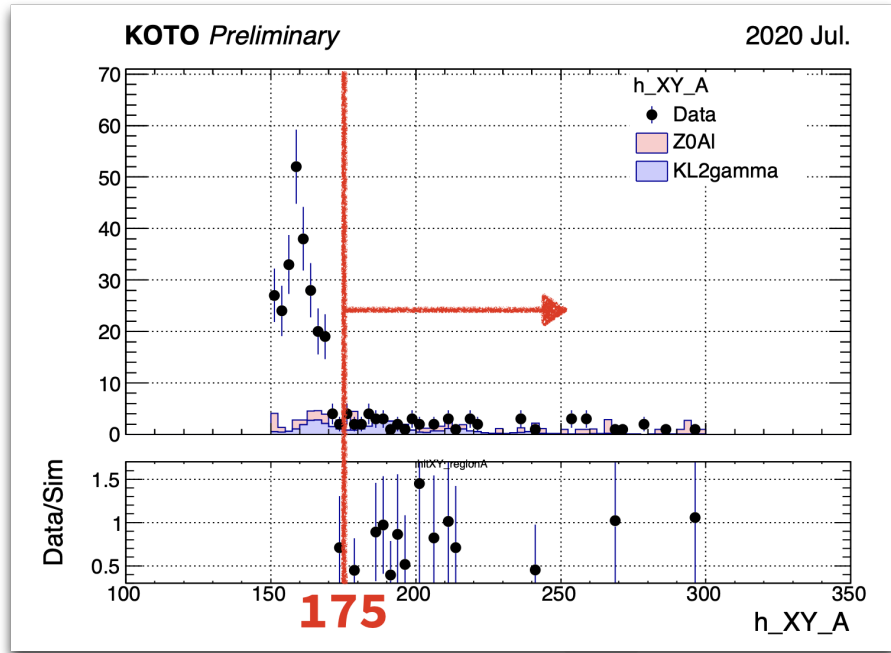


FIGURE 6.13: The R_{XY} distribution of the region 2. The red line and arrow indicated the cutoff region

⁴⁰⁹ **6.3.1 Systematic Uncertainty of SES**

⁴¹⁰ **6.4 Background Level Estimation**

⁴¹¹ Table 6.1 shows the background level of each background source in the signal region. The upper limit at 90% confidence level is estimated in the signal region.

TABLE 6.1: Number of events predicted for each source inside the signal region

Source		Number of events
K_L decay	$K_L \rightarrow 2\gamma$	1.09 ± 0.12
	$K_L \rightarrow 3\pi^0$	< 0.18 (90% C.L.)
	$K_L \rightarrow 2\pi^0$	< 0.51 (90% C.L.)
	$K_L \rightarrow \pi^\pm e^\mp \nu_e$	< 0.27 (90% C.L.)
	$K_L \rightarrow \pi^\pm \mu^\mp \nu_\mu$	< 0.25 (90% C.L.)
	$K_L \rightarrow \pi^+ \pi^- \pi^0$	< 0.17 (90% C.L.)
Neutron		11.57 ± 4.42

⁴¹²

⁴¹³ **6.5 Unblind and Results**

⁴¹⁴ **6.6 Massive Dark Photon Search**

⁴¹⁵ Chapter 7

⁴¹⁶ Conclusion and Discussion

⁴¹⁷ 7.1 blah

⁴¹⁸ blah blah blah

⁴¹⁹ Bibliography

- ⁴²⁰ [1] Andrzej J. Buras et al. " $K^+ \rightarrow \pi^+ \nu \bar{\nu}$ and $K_L \rightarrow \pi^0 \nu \bar{\nu}$ in the Standard Model: status
⁴²¹ and perspectives". In: *Journal of High Energy Physics* 2015.11 (Nov. 2015). DOI: [10.1007/jhep11\(2015\)033](https://doi.org/10.1007/jhep11(2015)033).
- ⁴²³ [2] Shoji Nagamiya. "Introduction to J-PARC". In: *Progress of Theoretical and Experimental
424 Physics* 2012.1 (Oct. 2012). 02B001. ISSN: 2050-3911. DOI: [10.1093/ptep/pts025](https://doi.org/10.1093/ptep/pts025).
- ⁴²⁵ [3] C. Lin. "Study of $K_L^0 \rightarrow \pi^0 \nu \bar{\nu}$ and $K_L^0 \rightarrow \pi^0 \gamma \gamma$ with the Cluster-Finding Trigger at
426 KOTO". National Taiwan University, 2021. DOI: [10.6342/NTU202102308](https://doi.org/10.6342/NTU202102308).
- ⁴²⁷ [4] Kota Nakagiri. "Search for the Decay $K_L^0 \rightarrow \pi^0 \nu \bar{\nu}$ at the J-PARC KOTO Experiment".
428 Ph.D. thesis. Kyoto University, 2019. DOI: [10.14989/doctor.k21564](https://doi.org/10.14989/doctor.k21564).
- ⁴²⁹ [5] Y. -C. Tung et al. "Suppression of neutron background using deep neural network
430 and Fourier frequency analysis at the KOTO experiment". In: *Nucl. Instrum. Meth. A*
431 1059 (2024), p. 169010. DOI: [10.1016/j.nima.2023.169010](https://doi.org/10.1016/j.nima.2023.169010).